nature geoscience

SUPPLEMENTARY INFORMATION

DOI: 10.1038/NGEO2427

Earthquake supercycle in subduction zones controlled by the width of the seismogenic zone

Robert Herrendörfer[1*], Ylona van Dinther[1], Taras Gerya[1] and Luis Angel Dalguer[2]

[1] Institute of Geophysics, ETH Zurich, Sonneggstrasse 5, CH-8092 Zurich, Switzerland

[2] swissnuclear, Aarauerstrasse 55, CH-4601 Olten, Switzerland

* robert.herrendoerfer@erdw.ethz.ch

Supplementary Methods 1: Numerical model

The numerical model setup (Supplementary Fig. 1) and material properties (Supplementary Table 2) are the same as in previous work[8] in which our seismo-mechanical numerical modelling approach was validated against laboratory subduction experiments[28]. The numerical and laboratory model setups are similar with respect to the geometry, model sizes and physical parameters (e.g., shear modulus, viscosity). The applied procedure to scale the results from this numerical model to nature is described in Supplementary Methods 2. In this model setup, a visco-elastic wedge is underthrusted by a rigid plate with a subduction velocity Vs of $3.9 \cdot 10^{-5} m \cdot s^{-1}$ (corresponds to 8.67 cm·yr^{-1} in nature, Supplementary Table 3) and at an angle α=10°.

We apply the continuum-based, two-dimensional, thermo-mechanical code I2ELVIS[8,26], which uses an implicit, conservative finite-difference scheme on a fully staggered Eulerian grid combined with a marker-in-cell technique. It solves for conservation of mass (eq. 1) and momentum (eq. 2-3) under the assumption of incompressibility:

$$\frac{\partial v_x}{\partial x} + \frac{\partial v_y}{\partial y} = 0 \tag{1}$$

$$\frac{\partial \sigma'_{xx}}{\partial x} + \frac{\partial \sigma'_{xy}}{\partial y} - \frac{\partial P}{\partial x} = \rho \frac{Dv_x}{Dt} \tag{2}$$

$$\frac{\partial \sigma'_{yx}}{\partial x} + \frac{\partial \sigma'_{yy}}{\partial y} - \frac{\partial P}{\partial y} = \rho \frac{Dv_y}{Dt} - \rho g \tag{3}$$

where v_x and v_y are horizontal and vertical velocities, σ'_{ij} are deviatoric stress tensor components, and g is gravitation acceleration. We neglect the influence of temperature.

A visco-elasto-plastic, constitutive relationship connects deviatoric stresses and strain rates $\dot{\varepsilon}'_{ij}$, applying linear elasticity and Newtonian viscosity:

$$\dot{\varepsilon}'_{ij} = \frac{1}{2G} \cdot \frac{D\sigma'_{ij}}{Dt} + \frac{1}{2\eta}\sigma'_{ij} + \begin{cases} 0 & \text{for } \sigma'_{II} < \sigma_{yield} \\ \chi \dfrac{\partial \sigma'_{II}}{\partial \sigma_{ij}} & \text{for } \sigma'_{II} = \sigma_{yield} \end{cases} \tag{4}$$

where G is shear modulus, η is effective viscosity, σ'_{II} ($\sqrt{\sigma'^2_{xx} + \sigma'^2_{xy}}$) is the second invariant of the deviatoric stress tensor, and χ is a plastic multiplier connecting plastic strain rates

and stresses. The megathrust is modelled as a frictional boundary layer, in which a non-associative Drucker-Prager plasticity[27] is applied. Plastic flow sets in when the plastic flow potential expressed by σ'_{II} reaches the local pressure-dependent yield strength σ_{yield}:

$$\sigma_{yield} = C + \mu_{eff} \cdot P \tag{5}$$

where C is cohesion and P is pressure. We apply a strongly rate-dependent friction[8], in which the effective friction coefficient μ_{eff} depends on the visco-plastic slip velocity V_{vp} ($\frac{\sigma_{yield}}{\eta_m} \cdot dx$, where η_m is the local viscosity from the previous time step and dx is the grid size):

$$\mu_{eff} = \mu_s(1-\gamma) + \mu_s \frac{\gamma}{1+\frac{V_{vp}}{V_c}} \tag{6}$$

where γ is amount of weakening ($1-\frac{\mu_d}{\mu_s}$), μ_s and μ_d are static and dynamic friction coefficients, respectively, and V_c is characteristic slip velocity. The seismogenic zone with downdip width W has velocity weakening properties (Supplementary Table 2). Velocity-strengthening and a low static friction is applied in the aseismic region.

We require a constant second invariant of deviatoric stresses during plastic deformation. This is related to the absence of elastic deformation:

$$\frac{D\sigma'_{II}}{Dt} = 0, \quad \dot{\varepsilon}'^{(elastic)}_{ij} = 0 \tag{7}$$

To fulfil that the yield strength is not exceeded, stresses are corrected in the following way:

$$\sigma'_{ij} = \sigma'_{ij} \frac{\sigma_{yield}}{\sigma'_{II}} \tag{8}$$

The total strain rate is the sum of the viscous and plastic strain rates, and a visco-plastic viscosity η_{vp} can be computed as follows:

$$\eta_{vp} = \eta \frac{\sigma'_{II}}{\eta\chi + \sigma'_{II}} \tag{9}$$

with

$$\chi = 2(\dot{\varepsilon}'_{II} - \dot{\varepsilon}'^{(vicous)}_{II}) = 2(\dot{\varepsilon}'_{II} - \frac{1}{2\eta}\sigma'_{II}) \tag{10}$$

where $\dot{\varepsilon}'_{II} = \sqrt{\dot{\varepsilon}^2_{xx} + \dot{\varepsilon}^2_{xy}}$. Thus the corrected viscosity η_{vp} is during plastic deformation:

$$\eta_{vp} = \frac{\sigma_{yield}}{2\dot{\varepsilon}'_{II}} \tag{11}$$

If the yielding condition is not fulfilled, $\eta_{vp} = \eta$.

Supplementary Methods 2: Scaling

Material properties (Supplementary Table 2), model dimensions and results of our numerical experiments are scaled up to natural values, following the scaling procedure as in previous work[8,28]. The scaling factors are given in Supplementary Table 3. The seismo-mechanical model is designed to be a scaled model of a natural subduction zone. Therefore, this model is designed to be geometrically, kinematically and dynamically similar to its natural prototype[31,32]. Geometrical similarity is achieved by introducing a consistent length scale L^*, which is the ratio between the characteristic lengths in the model and nature (e.g. downdip width of the seismogenic zone). Density and its ratio to the representative natural value yields the scaling factor ρ^*. Gravitation has the scaling factor $g^* = 1$ as it is the same in the model and nature. Kinematic and dynamic similarity requires that the ratio between a governing force in the model and in nature is a constant[32]. This constant is given by the ratio between gravitational forces in model and nature, which results in the universal force scaling factor F^*:

$$F^* = \frac{\rho_m \cdot L_m^3 \cdot g_m}{\rho_n \cdot L_n^3 \cdot g_n} = \rho^* \cdot L^{*3} \tag{12}$$

where the subscript m and n denote model and nature, respectively. This ratio needs to be the same for all other governing forces. From this, the scaling factor for stress σ^* can be derived:

$$\sigma^* = \frac{F^*}{L^{*2}} = \rho^* \cdot L^* \tag{13}$$

This scaling factor is also used for cohesion and shear modulus (Supplementary Table 3).

We adopt a dual time and velocity scale as in ref. 28 and 33. During the coseismic period, the ratio between inertial forces and gravitational forces needs to be same in model and

nature:

$$\frac{\rho_m \cdot v_m^2 \cdot L_m^2}{\rho_n \cdot v_n^2 \cdot L_n^2} = \frac{\rho_m \cdot L_m^3 \cdot g_m}{\rho_n \cdot L_n^3 \cdot g_n} = F^* \tag{14}$$

This equation yields the scaling factor v_c^* for the coseismic velocity:

$$v_c^* = \sqrt{\frac{\sigma^*}{\rho^*}} = \sqrt{L^*} \tag{15}$$

and consequently the coseismic time scaling factor T_c^*:

$$T_c^* = \frac{L^*}{v_c^*} = \sqrt{L^*} \tag{16}$$

In contrast, slow deformation processes are governed by viscous and gravitational forces during the interseismic period, while inertia is negligible. Thus, the ratio of these forces needs to be the same in model and nature:

$$\frac{\eta_m \cdot v_m \cdot L_m}{\eta_n \cdot v_n \cdot L_n} = \frac{\rho_m \cdot L_m^3 \cdot g_m}{\rho_n \cdot L_n^3 \cdot g_n} = F^* \tag{17}$$

This results in the following equation:

$$\eta^* \cdot v_s^* = \rho^* \cdot L^{*2} \tag{18}$$

This equation needs to be fulfilled with two unknown scaling factors for the interseismic velocity v_s^* and for the viscosity η^*. From these, v_s^* can be better constrained as the ratio between the loading velocity in the laboratory-scaled model setup and the subduction velocity in nature (Supplementary Table 3). From this we obtain the viscosity scaling factor η^*:

$$\eta^* = \frac{\rho^* \cdot L^{*2}}{v_s^*} \tag{19}$$

and interseismic time scaling factor T_i^*:

$$T_i^* = \frac{L^*}{v_s^*}. \tag{20}$$

Supplementary Methods 3: Picking algorithm

Events are selected using measurements of the horizontal velocity V at 1 cm (up-scaled to nature:$\sim$6.37 km, Supplementary Table 3) above the frictional boundary layer[8,28]. If the maximum of V is larger than the velocity threshold of 0.015 cm/s (up-scaled to nature: 0.12 m/s, Supplementary Table 3) inside the limits of the seismogenic zone, an event is picked. We slightly updated the event selection criteria of ref. 8 and 28 so that an event consists of at least five time steps larger than the velocity threshold and is separated by 20 time steps from another event. The start of an event t_i is set at 15 time steps before the velocity threshold is reached to capture the initial stress state prior to the nucleation of the event. The end of an event is defined at time step t_f, once the maximum of the horizontal velocity falls below the threshold.

A lower velocity threshold would include more smaller events, which are mostly sub-critical ruptures that nucleate close to the seismogenic zone limits. However, the general conclusions are not affected by a lower velocity threshold.

Supplementary Methods 4: Analysed functions and parameters

We evaluate the different models by analysing a set of functions at each time step t and event parameters, which are averaged over the width W of the seismogenic zone. Coordinates d and u define the downdip and updip limit, respectively. Stresses and strength are measured directly at the top of the frictional boundary layer.

1. Cumulative sum of displacements D:

$$D(t) = \frac{1}{W} \sum_{j=1}^{t} \sum_{x=d}^{u} V(x,j) \cdot \Delta t \cdot \Delta x \tag{21}$$

   This function tracks the evolution of the accumulated elastic strain within the seismogenic zone. The trend is removed.

2. Strength excess SE:

$$SE(t) = \frac{1}{W} \sum_{x=d}^{u} (\sigma_{yield}(x,t) - \sigma'_{II}(x,t)) \cdot \Delta x \tag{22}$$

It represents the stress and strength state in the seismogenic zone. Low values indicate that the entire seismogenic zone is close to a critical state at which system-wide events are prone to develop.

3. Stress change SC is the difference between final and initial stress:

$$SC = \frac{1}{W}\sum_{x=d}^{u}(\sigma'_{II}(x,t_f) - \sigma'_{II}(x,t_i)) \cdot \Delta x \tag{23}$$

4. S parameter for each event:

$$S = \frac{SE(t_i)}{SC} \tag{24}$$

The median S parameter is the median value of all selected events in a model.

5. Characteristic recurrence interval or average supercycle interval Tc:

$$Tc = \frac{1}{f(max(FFT(D(t)))} \tag{25}$$

Inverse of the frequency at the maximum of the fourier spectrum obtained from $D(t)$. This parameter depicts the average recurrence interval between the largest events in a model. Assuming smaller events in between these superevents, Tc represents the average interval of a supercycle.

6. Number of events per supercycle NS:

$$NS = NT \cdot \frac{Tc}{T} \tag{26}$$

where NT is total number of events during the model duration T (excluding the first 100 seconds).

Supplementary Discussion 1: Estimates of the seismogenic zone downdip width

The estimates of reference 5 and 6 are one constraint on the seismogenic zone downdip width from the hypocenter locations of moderate thrust interface earthquakes that is available for most subduction zones. They mainly differ between each other in that ref. 5 assumes a pla-

nar geometry and determines both the up-and downdip limit of the seismogenic zone, while ref. 6 accounts for a non-planar geometry and determines only the depth of the downdip limit. Both estimates provide each an average width value for a subduction segment, which might be not representative in those regions with considerable along-strike variations. We believe, however, that both studies provide consistent and comparable first-order estimates of the downdip width of the seismogenic zone where currently many interface thrust earthquakes occur. In those subduction zones, these estimates agree reasonably well with other constraints. For instance, in NE Japan, width values from interseismic locking ($\sim$ 150 km, ref. 34) and fault mechanism of small earthquakes ($\sim$ 160 km, ref. 35-36) are consistent with 161 km given by ref. 5 and 162 km given by ref. 6 (Supplementary Table 1). For Sumatra, their width estimates of 159 km (ref. 6) and 175 km (ref. 5) agree with thermal and structural constraints ($\sim$ 156 km, ref. 37), geodetic estimates ($\sim$ 175 km, ref. 38), downdip rupture widths estimates ($\sim$ 175 km, ref. 39), and an interpretation of a local earthquake tomography study ($\sim$ 200 km ref. 40).

In Cascadia, the method of ref. 5 and ref. 6 does not work as well due to the scarcity of interface thrust earthquakes. While ref. 6 does not consider Cascadia at all, ref. 5 listed a width constrained by thermal data[41]. There is a wide range of estimates and room for interpretation of what defines the actual seismogenic zone downdip width in Cascadia. Discussion and uncertainties remain amongst others about (1) the depth of the thermal limits of 350° C and 450° C (ref. 41-42) for example in light of hydrothermal cooling[43], (2) the width of the transition zone between the geodetically inferred locked zone and freely slipping part, especially considering the change in seismic reflection character with depth[44]. Also, width estimates vary significantly from North to South[41−42], which might lead to a different cycle behaviour (see Supplementary Results).

In Southern Chile, the seismogenic zone downdip width is not well constrained from thrust earthquakes locations alone. Ref. 5 used thermal constraints from ref. 40, while ref. 6 stated a poorly constrained width of 105 km. The latter does not agree with larger estimates from thermal limits: 160 km (ref. 45), 159-220 km (ref. 46) and 200 km (ref. 47). These latter values indicate a rather wide downdip extent of the seismogenic zone, at least as wide as the value given in Supplementary Table 1.

Supplementary Discussion 2: Recurrence interval and displacements

The scaled recurrence intervals in our numerical models (Fig. 2, Supplementary Fig. 2) are long compared to expected values in nature. The scaled recurrence interval is influenced by (i) mainly a small scaled shear modulus of the visco-elastic wedge originating from the simulated laboratory model[8,28] (Supplementary Table 2), (ii) the choice of frictional parameters μ_s and γ (Supplementary Fig. 3), and (iii) the model restriction to two dimensions. The same holds for the scaled displacements, which are larger than expected in nature.

Supplementary Results: Case studies

We performed additional numerical experiments to analyse simplified models of subduction zones in NE Japan, southern Chile, Sumatra and Cascadia. In these subduction zones, supercycles have been proposed (see main text). For the first three models, we take for each subduction zone the geometric parameters of the seismogenic zone (downdip width W, downdip depth Dz and subduction angle) and subduction velocity that are given in ref. 5, while all other parameters remain the same. Results show that supercycles evolve in these models of Sumatra, S Chile and NE Japan (Supplementary Fig. 4a-c) in which the estimated seismogenic zone downdip width is in reasonable agreement with other constraints (see Supplementary Discussion 1). For Cascadia, where the width estimates vary significantly along the strike[41−42], we show the model outcome for two cases. The model with a potentially narrower seismogenic zone (case A) is characterized by ordinary cycles (Supplementary Fig. 4d). This might be representative for the long-term seismicity in southern part of Cascadia, where the seismogenic zone is estimated to be quite narrow[41−42]. In contrast, supercycles evolve in model case B with a larger than average seismogenic zone width (Supplementary Fig. 4e), which is potentially representative for northern Washington. This difference between case A and B indicates that a 3D model is desired to study the role of along-strike variations in downdip width for the long-term seismicity.

Supplementary Figures and Captions

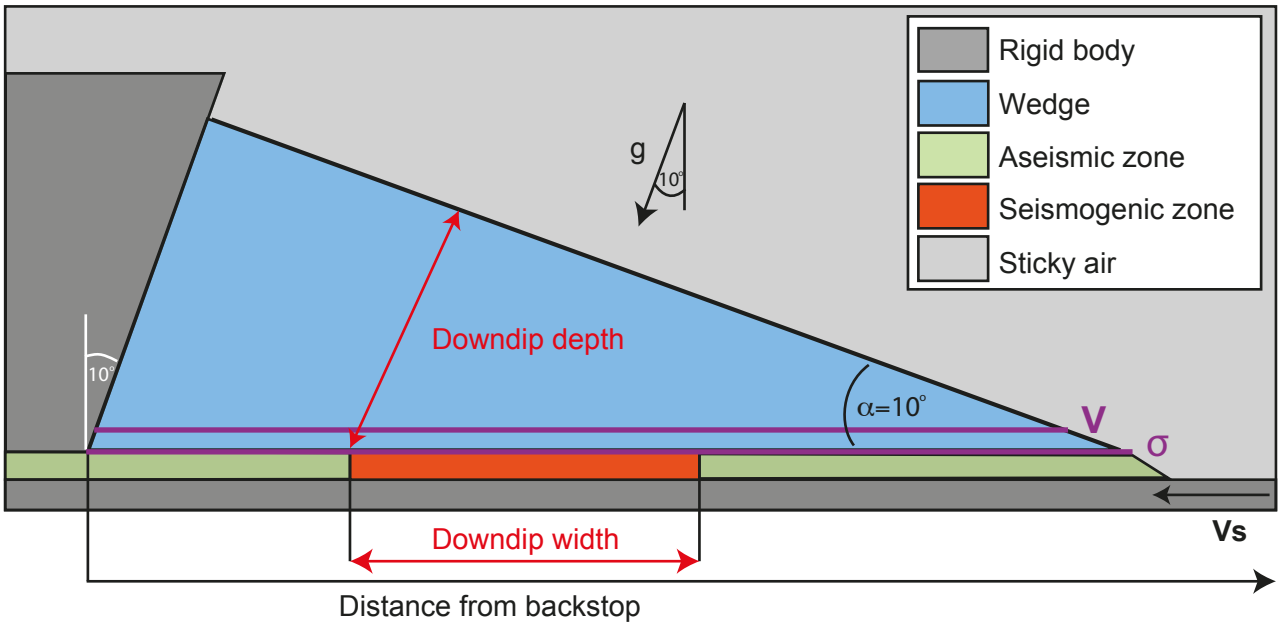

Supplementary Figure 1 | Numerical model setup. Colours show different model entities. Vs denotes subduction velocity. Horizontal displacement velocity V is measured 1 cm above, stress and strength at the top of the frictional boundary layer (purple lines). Model setup and gravitation vector g are rotated around the subduction angle of $\alpha = 10°$.

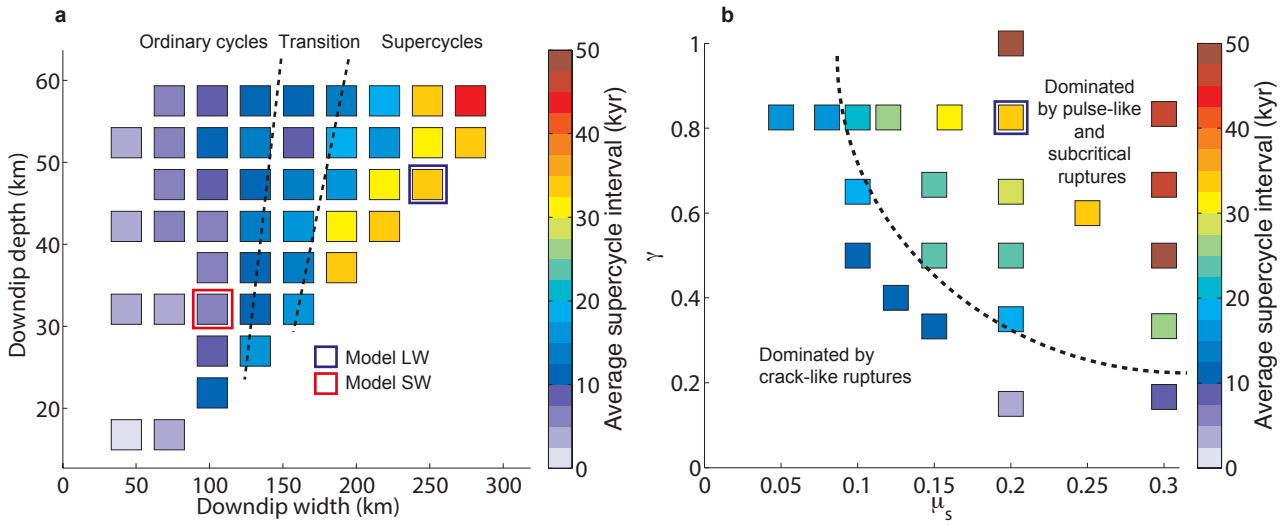

Supplementary Figure 2 | Average supercycle interval. Characteristic recurrence time (Supplementary Methods 4) as a function of **a**, the downdip width and depth of the seismogenic zone, and **b**, as a function of the static friction coefficient and the relative friction drop γ ($= \frac{\mu_s - \mu_d}{\mu_s}$). Blue frame indicates reference model LW.

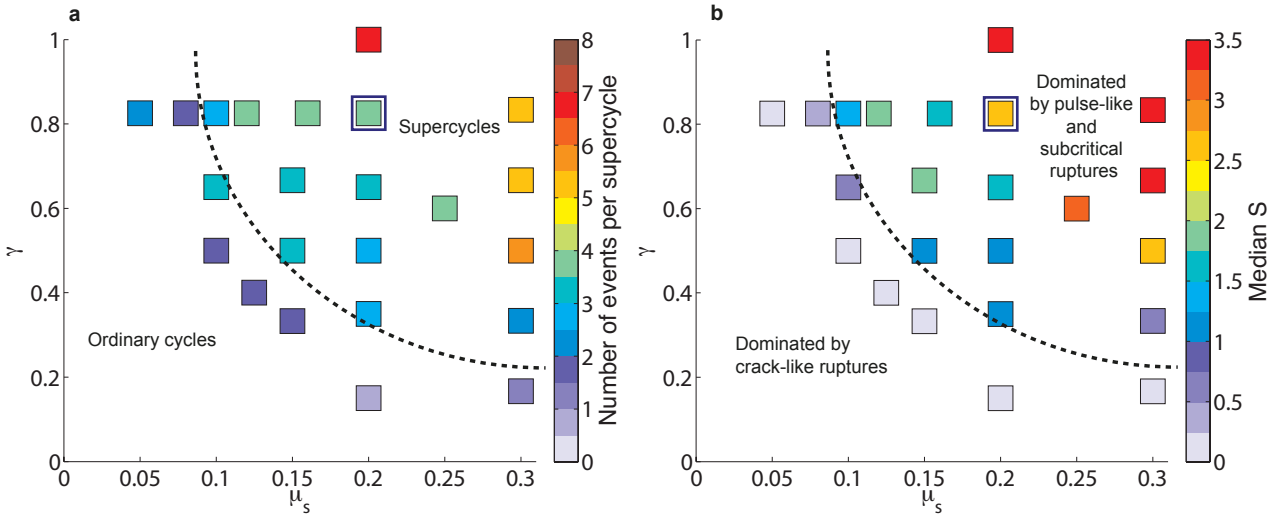

Supplementary Figure 3 | Influence of friction parameter. Influence of static friction μ_s and relative friction drop γ ($= \frac{\mu_s - \mu_d}{\mu_s}$) on **a**, the number of events per supercycle and, **b**, median S parameter in model LW (blue frame). Dashed line roughly indicates the transition between ordinary cycles and supercycles in **a,** and between the dominance of crack-like and pulse-like ruptures in **b**.

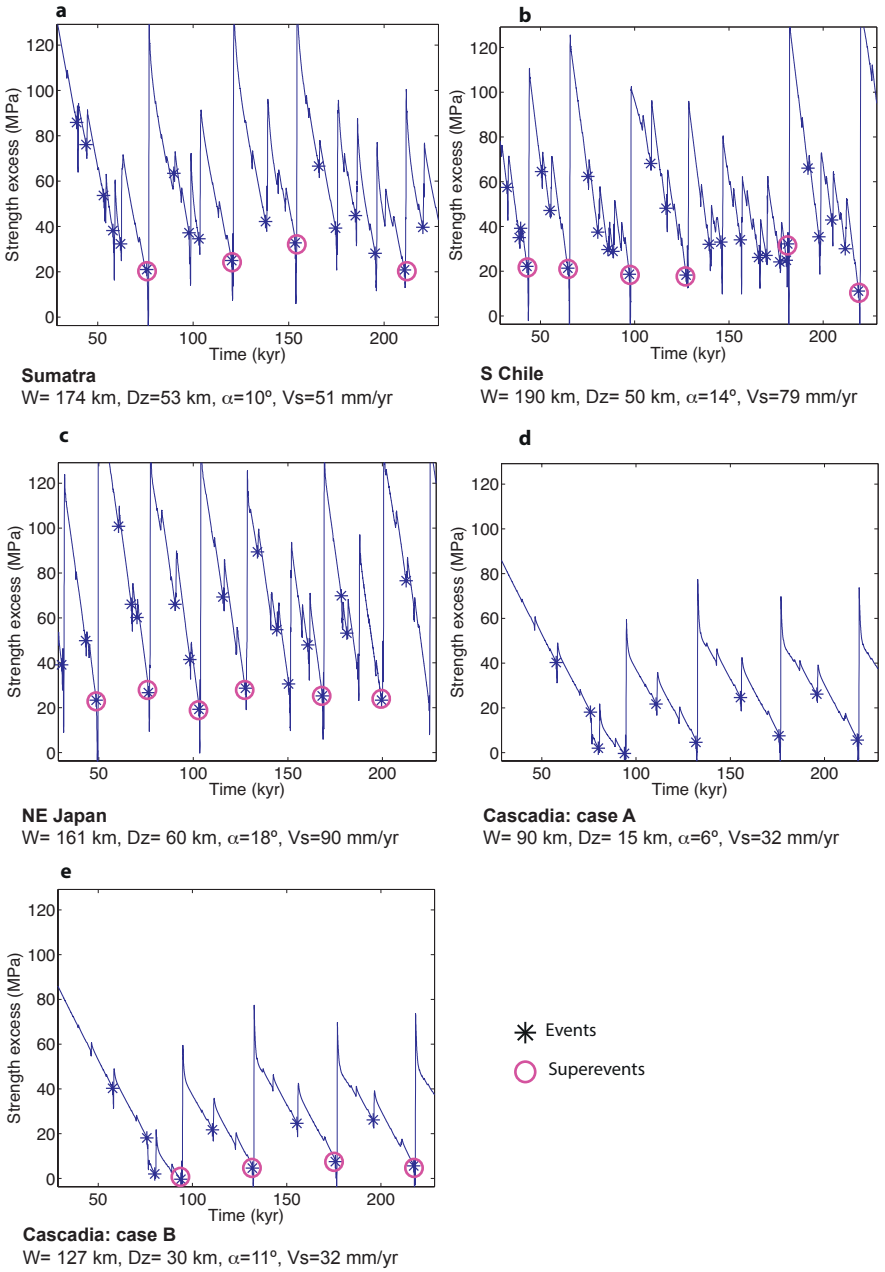

Supplementary Figure 4 | Supercycles in case studies. Strength excess as a function of time in simplified subduction zone models of **a**, Sumatra, **b**, southern Chile, **c** north-east Japan, **d**, Cascadia (case A), and **e**, Cascadia (case B). Model parameters are given for each case study: seismogenic zone downdip width (W) and depth (Dz), subduction angle α and subduction velocity Vs. The initial time (50-150 kyr) corresponds to the transition to steady state seismic behaviour of the model.

Supplementary Table 1 | Global downdip width estimates. Estimates of the seismogenic zone downdip width[5–6]. Average of both estimates is given and visualised in Fig. 1. Definition of subduction zone segments follows reference 5. For values denoted by *, ref. 5 uses thermal constraints from ref. 41. Ref. 6 is extended by a regional study of the Antilles[7].

Subduction zone segment	ref. 5 W (km)	ref. 6-7 W (km)	Average W (km)
Andaman	243	159	201
Sumatra	174	159	166.5
Java	188	173	180.5
Philippines	81	79	80
S-Ryukyu	73	116	94.5
N-Ryukyu	122	116	119
Nankai	132*	116	124
Marianas	93	85	89
IzuBonin	104	85	94.5
Japan	161	162	161.5
S-Kuril	102	148	125
N-Kuril	95	137	116
Kamchatka	110	150	130
Ws-Aleutians	72	108	90
C-Aleutians	75	139	107
E-Aleutians	72	130	101
W-Alaska	91	151	121
E-Alaska	180	151	165.5
Mexico	74	73	73.5
Costa Rica	103	83	93
Cocos	138	83	110.5
Colombia	101	128	114.5
N-Peru	118	128	123
S-Peru	79	133	106
N-Chile	105	143.5	124.25
S-Chile	190*	105	147.5
Antilles	168	120	144
Sandwich	131	68	99.5
S-Kermadec	117	119	118
N-Kermadec	112	119	115.5
S-Tonga	80	101	90.5
N-Tonga	98	101	99.5
S-New Hebrides	83	70	76.5
D'Entrecasteaux	72	70	71
N-NewHebrides	100	70	85
Salomon Islands	87	62	74.5
Bougainville	97	62	79.5
New Britain	121	101	111
Hikurangi	178		178
Cotobato	52		52
Flores	57		57
W-Aegean	179		179
Cascadia	127*		127
Timor	110		110
Seram	76		76
Halmahera	79		79
Sangihe	104		104
Sulawesi	62		62
Manila	98		98
Mean Value	**112**	**113**	**111**

Supplementary Table 2 | Material parameters. Material parameters are adopted from ref. 8. Given values are upscaled from these model properties to natural values following scaling relations (Supplementary Methods 2, Supplementary Table 3), using a dual time scale for the interseismic and coseismic period. The characteristic velocity V_c is scaled with the coseismic time scale. Values denoted by * are corrected by a displacement reduction factor of 100 (ref. 8). This factor is applied to reduce the amount of displacements near the toe of the wedge. Viscosity and shear modulus are increased by this factor, while the time step is reduced by it to keep stresses and velocities the same.

Parameter	Symbol	Unit	Wedge	Seis. zone	Aseis. zone	Rigid body	Sticky air
Min. viscosity	η_{min}	Pa·s	$5{\cdot}10^{21*}$	$1.7{\cdot}10^{14*}$	$1.7{\cdot}10^{14*}$	$1.7{\cdot}10^{22*}$	$3.3{\cdot}10^{13*}$
Max. viscosity	η_{max}	Pa·s	$5{\cdot}10^{21*}$	$5{\cdot}10^{21*}$	$5{\cdot}10^{21*}$	$1.7{\cdot}10^{22*}$	$3.3{\cdot}10^{13*}$
Shear modulus	G	GPa	9.2^*	9.2^*	9.2^*	$2.95{\cdot}10^{9*}$	9.2^*
Density	ρ	$kg{\cdot}m^{-3}$	2900	2900	2900	2900	2.9
Static friction	μ_s	-	-	0.2	0.002	-	-
Dynamic friction	μ_d	-	-	0.035	0.157	-	-
Char. velocity	V_c	$m{\cdot}s^{-1}$	-	0.16	0.031	-	-
Cohesion	C	MPa	-	11.1	11.1	-	-

Supplementary Table 3 | Scaling factors $(*)$[28], converting model values (P_M) to natural values (P_N). Examples are given for key input parameters and model results.

Parameter	Scaling factor	P_M/P_N	P_M	P_N
Gravity acceleration	g^*	1	9.81 m·s^{-2}	9.81 m·s^{-2}
Density	ρ^*	0.345	1000 kg·m^{-3}	2900 kg·m^{-3}
Length	L^*	$1.57{\cdot}10^{-6}$	0.16 m	101.9 km
Stress	σ^*	$5.42{\cdot}10^{-7}$	60 Pa	111 MPa
Cohesion	σ^*	$5.42{\cdot}10^{-7}$	6 Pa	11.1 MPa
Shear modulus	σ^*	$5.42{\cdot}10^{-7}$	5000 Pa	9.2 GPa
Coseismic time step	T_c^*	$1.25{\cdot}10^{-3}$	0.066 s	53 s
Coseismic duration	T_c^*	$1.25{\cdot}10^{-3}$	1.84 s	24.5 min
One-sided slip velocity	v_c^*	$1.25{\cdot}10^{-3}$	$0.082{\cdot}10^{-2}$ m·s^{-1}	0.65 m·s^{-1}
Velocity threshold	v_c^*	$1.25{\cdot}10^{-3}$	0.015 cm·s^{-1}	0.12 m·s^{-1}
Interseismic velocity	v_s^*	$1.42{\cdot}10^{4}$	$3.9{\cdot}10^{-5}$ m·s^{-1}	8.67 cm·yr^{-1}
Viscosity	η^*	$6.0{\cdot}10^{-17}$	$3{\cdot}10^{5}$Pa·s	$5{\cdot}10^{21}$Pa·s
Interseismic time step	T_i^*	$1.11{\cdot}10^{-10}$	0.066 s	18.8 yr
Interseismic duration	T_i^*	$1.11{\cdot}10^{-10}$	19.3 s	5518 yr

Main text references

[5] Heuret, A., Lallemand, S., Funiciello, F., Piromallo, C. & Faccenna, C. Physical characteristics of subduction interface type seismogenic zones revisited. *Geochem., Geophys., Geosys.* **12,** Q01004 (2011).

[6] Hayes, G.P., Wald, D.J. & Johnson, R.L. Slab1.0: A three-dimensional model of global subduction zone geometries. *J. Geophys. Res.* **117,** B01302, (2012).

[7] Hayes, G. P., McNamara, D. E., L. Seidman, L., & Roger, J. Quantifying potential earthquake and tsunami hazard in the Lesser Antilles subduction zone of the Caribbean region. *Geophys. J. Int.* **196,** 510–521 (2013).

[8] van Dinther, Y. *et al.* The seismic cycle at subduction thrusts: 2. Dynamic implications of geodynamic simulations validated with laboratory models. *J. Geophys. Res.: Solid Earth*, **118,** 1502–1525 (2013).

[26] Gerya, T.V. & Yuen, D.A. Robust characteristics method for modelling multiphase visco-elasto-plastic thermo-mechanical problems. *Phys. Earth Planet. Inter.* **163**, 83–105 (2007).

[27] Drucker, D.C. & Prager, W. Soil mechanics and plastic analysis of limit design. *Quarterly of Applied Mathematics* **10,** 157–165 (1952).

[28] Corbi, F. *et al.* The seismic cycle at subduction thrusts: 1. Insights from laboratory models. *J. Geophys. Res.: Solid Earth* **118,** 1483–1501 (2013).

[29] van Dinther, Y. *et al.* The seismic cycle at subduction thrusts: Insights from seismo-thermo-mechanical models. *J. Geophys. Res.: Solid Earth*, **118,** 6183–6202 (2013).

Supplementary references

[31] Hubbert, M.K. Theory of scale models as applied to the study of geological structures. *Geol. Soc. Am. Bull.* **48,** 1459–1520 (1937).

[32] Ramberg, H. Gravity, deformation and the earth's crust as studied by centrifued models. (Academic Press, London, 1967)

[33] Rosenau, M., Lohrmann, J. & Oncken, O. Shocks in a box: An analogue model of subduction earthquake cycles with application to seismotectonic forearc evolution. *J. Geophys. Res.* **114,** B01409 (2009).

[34] Loveless, J.P. & Meade, B.J. Geodetic imaging of plate motions, slip rates, and partitioning of deformation in Japan. *J. Geophys. Res.* **115,** B02410 (2010).

[35] Igarashi, T., Matsuzawa, T., Umino, N. & Hasegawa, A. Spatial distribution of focal mechanisms for interplate and intraplate earthquakes associated with the subducting Pacific plate beneath the northeastern Japan arc: A triple-planed deep seismic zone. *J. Geophys. Res.* **106,** 2177–2191 (2001).

[36] Seno, T. Variation of downdip limit of the seismogenic zone near the Japanese islands: implications for the serpentinization mechanism of the forearc mantle wedge. Earth Planet. Sci. Lett. **231,** 249-262 (2005).

[37] Hippchen, S. & Hyndman, R. D. Thermal and structural models of the Sumatra subduction zone: Implications for the megathrust seismogenic zone. *J. Geophys. Res.* **113,** B12103 (2008).

[38] Chlieh, M., Avouac, J. P., Sieh, K., Natawidjaja, D. H. & Galetzka, J. Heterogeneous coupling of the Sumatran megathrust constrained by geodetic and paleogeodetic measurements. *J. Geophys. Res. Solid Earth* **113,** B05305 (2008).

[39] Zachariasen, J., Sieh, K., Taylor, F.W., Edwards, R. W. & Hantoro, W. S. Submergence and uplift associated with the giant 1833 Sumatran subduction earthquake: Evidence from coral microatolls. *J. Geophys. Res.* **104,** 895–919 (1999).

[40] Collings, R. *et al.* Structure and seismogenic properties of the Mentawai segment of the Sumatra subduction zone revealed by local earthquake traveltime tomography. *J. Geophys. Res.* **117,** B01312 (2012).

[41] Oleskevich, D. A., Hyndman, R. D. & Wang, K. The updip and downdip limits to

great subduction earthquakes: Thermal and structural models of Cascadia, south Alaska, SW Japan, and Chile *J. Geophys. Res.* **104,** 14965–14991 (1999).

[42] Hyndman, R. D. & Wang, K.. The rupture zone of Cascadia great earthquakes from current deformation and the thermal regime. *J. Geophys. Res.* **100,** 22133-22154 1995.

[43] Cozzens, B. D. and Spinelli, G. A. A wider seismogenic zone at Cascadia due to fluid circulation in subducting oceanic crust. *Geology* **424,** 899–902 (2012).

[44] Nedimović, M.R., Hyndman, R.D., Ramachandran, K. & Spence, G. D. Reflection signature of seismic and aseismic slip on the northern Cascadia subduction interface. *Nature* **424,** 416–420 (2003).

[45] Wang, K. *et al.* Crustal motion in the zone of the 1960 Chile earthquake: Detangling earthquake-cycle deformation and forearc-sliver translation. *Geochemistry, Geophys. Geosystems* **8,** Q10010 (2007).

[46] Völker, D., Grevemeyer, I., Stipp, M., Wang, K. & He, J. Thermal control of the seismogenic zone of southern central Chile. *J. Geophys. Res.* **116,** B10305 (2011).

[47] Rotman, H. M. M. & Spinelli, G. A. Remarkably consistent thermal state of the south central Chile subduction zone from 36° S to 45° S. *J. Geophys. Res. Solid Earth* **119,** 3503–3516 (2014).